JNTM JOURNAL of NEW TECHNOLOGY and MATERIALS

Journal of New Technology and Materials

Vol. 15, No. 1 (2025), 23–35

RESEARCH ARTICLE

Electrolyte-Resolved Voltage-Gated Inventory Reconstruction of Manganese Dissolution from Spinel $LiMn_2O_4$ Cathodes

Ioanna Kakoulli[1,*] and Yumin Du[1]

[1]Materials Science and Engineering, University of California, Los Angeles, CA 90095, USA

*Correspondence: kakoulli@ucla.edu

Received date: January 10, 2025; Accepted date: May 12, 2025

Abstract

Dissolution of manganese from the $LiMn_2O_4$ cathode material has been shown to be another significant barrier in high-voltage lithium ion batteries, since it links surface redox instability, electrolyte breakdown, dissolution of transition metals, and ensuing interphase instability. Current post mortem methods based on simple chemical assays give accurate estimates of total manganese but do not provide details about the start of dissolution, redistribution of the released Mn^{2+} species within the electrolyte, and the effect of the electrolyte chemistry on the voltage window where dissolution occurs. In this paper, a voltage-gated electrolyte-resolved reconstruction technique is proposed, which considers the proton magnetic resonance imaging (PMRI) data as electrolyte-based manganese inventory information. It includes concentration calibration from the image intensity, assignment of concentration change to specific voltages, spatial segmentation of the electrolyte into three compartments close to the cathode, central region, and anode side, and calculation of inventory descriptors accounting for spatial concentration versus molar inventories. The analysis of the PMRI data obtained for $LiMn_2O_4$ cells containing 1 M $LiPF_6$ EC:DMC liquid electrolyte, $LiPF_6$ EC:DMC gel electrolyte, and 1 M LiTFSI methyl-3-cyanopropanoate electrolyte reveals the appearance of manganese release gate at 4.1 V, an increased rate of manganese dissolution in the high voltage regime beyond 4.7 V, and the map-based maximal concentration of Mn^{2+} in the gel electrolyte region of 36 µmol L^{-1}. Reconstruction of regional manganese inventories results in the values of 8.42×10^{-10}, 6.51×10^{-10}, and 8.45×10^{-10} mol for cathode, middle, and anode electrolyte regions, leading to the total first cycle value of 2.34×10^{-9} mol. Despite having a smaller local concentration, the anode side compartment has a similar molar inventory because of larger electrolyte volume in this region, proving that concentration gradient does not correlate with degradation potential. Suppression of charge window intensity rise in the cyanester-LiTFSI electrolyte suggests that the latter prevents voltage gate manganese dissolution process instead of lowering the final dissolved manganese concentration.

Keywords: lithium-ion battery, spinel cathode, $LiMn_2O_4$, manganese dissolution, magnetic-resonance imaging, electrolyte chemistry, transition-metal migration, voltage-gated inventory

1 Introduction

Spinels $LiMn_2O_4$ stand out among manganese-based cathodes of lithium-ion batteries due to their relatively high abundance of component elements, fast three-dimensional lithium diffusion through the spinel structure, operating potential close to the 4 V range, and a generally affordable production strategy as opposed to expensive and complex layer oxide cathodes that are rich in cobalt. The high voltage required to extract lithium from the spinel lattice leads to significant capacity fading under repeated cycling, and the magnitude of fading worsens with elevated temperature, aggressive electrolyte chemistry, and presence of strong acids produced by salt and organic solvent breakdown. In general, high-voltage cycling of spinel $LiMn_2O_4$ is characterized by surface manganese redox changes, electrolyte oxidation, and migration of transition metals, but the precise mechanism and dynamics remain uncertain due to lack of direct experimental evidence. Spinel oxides are particularly interesting to study because of their unique electrochemical behaviour, where surface redox chemistry and manganese release are linked directly to the electrolyte chemistry and metal transport properties.

It should be noted that the literature describing spindel manganese oxides indicates that the phenomenon of capacity fading cannot be attributed to a particular single failure event. Electrochemical characterization pointed to the structural redox changes in the spinel lattice, and spectroscopic measurements and electrolyte dependence highlighted the critical roles of salt chemistry, acid environment, and metal transport capability in manganese dissolution [1–3]. This knowledge base is relevant to the present work because the dissolved manganese signal was considered here not as the final residual concentration but as a spatiotemporally varying degradation pathway.

Manganese dissolution from the cathode in a carbonate electrolyte is a well-known mechanism responsible for the degradation of spindel-based cathode materials. It typically proceeds through chemical interaction of the exposed delithiated spinel surface and electrolyte, or surface redox of manganese and disproportionation of surface Mn^{3+} ions into solvated Mn^{2+} ions [4, 5]. Under carbonate $LiPF_6$-based electrolyte, the dissolution is significantly facilitated by the formation of acidic species, such as HF, through water content and salt decomposition, and the liberated manganese ions diffuse through the electrolyte toward the anode. Besides serving as a loss of active cathode material, the dissolved manganese ions become the interfacial contaminants, and they can alter SEI composition, increase electrolyte impedance, catalyze unwanted electrolyte reactions, and increase the irreversible lithium consumption.

Electrochemical experiments, post-mortem characterization, and in situ X-ray imaging indicate that the extent of manganese release can be dependent on electrode voltage and electrolyte formulation, but at the same time demonstrate the need for detailed spatial analysis [5, 6]. Atomistic and mechanistic studies, in addition, suggest that both electrolyte solvent decomposition and surface redox instability facilitate manganese dissolution, and the process of disproportionation provides a chemical pathway to solubilize lattice manganese and produce Mn^{2+} ions [7, 8]. The current state-of-the-art knowledge answers the question about the source of manganese dissolution. However, the diagnostics still face unresolved challenges of identifying the voltage interval, final position, and molar amount of the released manganese ions during the electrochemical cycle.

The traditional approaches used to investigate manganese release rely mainly on ex situ and bulk analyses of dissolved manganese, including ICPS or chromatography. They allow establishing the total amount of dissolved manganese ions based on a specific electrochemical cycling protocol. But the conventional techniques are unable to answer three important questions: when the dissolution started, where it occurred, and how the released manganese is partitioned between the cathode-proximal and anode-proximal regions of the cell. Furthermore, it is not possible to understand from these techniques alone how an added electrolyte affects manganese dissolution, whether it slows down the process, reduces manganese concentration, or inhibits its transport. This is the reason why there is a need for spatially sensitive measurements that preserve the information recorded during cell operation.

These objectives can be fulfilled by nuclear magnetic resonance and magnetic resonance imaging, as it allows probing battery systems in operando and sensitive to ion distribution, electrolyte transport, and presence of paramagnetic species. ^{7}Li MRI is shown to image lithium distribution and salt gradient, and ^{1}H MRI was found to respond to dissolution of manganese [9, 10]. Previous magnetic resonance studies demonstrate the viability of electrochemical measurements by MRI and reveal a possibility of imaging the processes involving electrochemical cycling, metal dissolution, and local transport [11, 12]. Dissolution of manganese in particular is relevant for ^{1}H imaging, because Mn^{2+} is a paramagnetic ion and affects the relaxation of protons in the solution. By comparing the proton intensity with a known manganese concentration, MRI results can be calibrated to provide not only contrast, but also the concentration distribution.

Recent studies also indicate the ability of MRI to quantify paramagnetic relaxation due to dissolved transition metals in the electrolyte [13]. Therefore, building on previous knowledge, this work uses proton MRI to estimate and analyze molar amounts of dissolved manganese in an electrolyte. This technique preserves a wealth of information, as it allows following manganese dissolution not only as an increased signal but also tracking the voltage window when the process occurs and the electrolyte regions where manganese is concentrated.

As indicated before, a signal increase alone is not enough to establish a full picture of manganese dissolution. High concentration near the cathode confirms its release origin, while a distributed signal with lower concentration can carry a similar or even higher number of moles. Moreover, it is impossible to tell from a final concentration map when manganese was released and what voltage controlled its release rate. Therefore, it is desirable to link the MRI measurement data with the actual molar concentration, segmented electrolyte volume, and applied voltage history to provide an integrated picture of the phenomenon. That is the reason for developing the present voltage- and electrolyte-resolved reconstruction algorithm of the molar manganese inventory.

Manganese dissolution is modeled as a joint process of materials, electrolyte, and transport. The first step is calibration of the proton MRI intensity to Mn concentration, the second step is assigning measured concentrations to voltage domains, and the third step is partitioning of the electrolyte into regions according to their proximity to the cathode and calculating the amount of manganese inside. Such approach goes beyond mere image visualization and attempts to quantify molar inventories of manganese in cathode-proximal, middle, and anode-proximal reservoirs. This method answers questions about how much manganese is released, where it is located, what is the voltage window controlling its release, and how electrolyte chemistry alters dissolution.

From the point of view of materials science and engineering, the significance of the work relies on the direct applicability to lithium battery stability and electrolyte development. Improvement in cycling lifetime of the spinel $LiMn_2O_4$ requires

stabilization of the crystal structure and suppression of the electrolyte-based pathways that lead to manganese dissolution. Novel types of electrolytes have been introduced for 4 V batteries to minimize the problems related to corrosion, such as cyanoesters and alternative salts, whereas gel electrolytes can potentially decrease convective mixing and simplify interpretation of concentration gradients [14, 15]. By comparing results obtained with carbonate-$LiPF_6$, gel-cyanoester-$LiPF_6$, and cyanoester-LiTFSI, the present study establishes connections between electrolyte formulation and suppression of voltage-triggered manganese dissolution.

Furthermore, the electrolyte literature emphasizes the necessity to consider interactions between the solvent, salt, and SEI to ensure passivation instead of electrolyte decomposition under high-voltage cycling [16]. This is especially true for electrolytes used to protect spindels against manganese release. Consequently, it makes sense to evaluate protective electrolyte not only based on final capacity retention or dissolved metal amount but also according to its ability to delay the release start, shorten its voltage window, or prevent manganese transport toward interphase-sensitivie regions. This paper considers different electrolytes as variables affecting not only generation but also transportation of dissolved Mn^{2+}.

Thus, the major question of this research is whether the manganese dissolution in spinel $LiMn_2O_4$ can be mapped as a voltage-resolved inventory process and not just a concentration change or an MRI image. The answer is confirmed by the presented tables and graphs: manganese release starts near 4.1 V, accelerates above 4.7 V, results in non-uniform but inventory-significant concentration distribution, and demonstrates distinct features of dissolution phenotypes in different electrolytes.

2 Materials Basis and Analytical Method

2.1 Measured values used for reconstruction

The reconstruction uses published measurements by Hellar and co-workers for electrode formulation, electrolyte identities, galvanostatic current, magnetic-resonance acquisition conditions, calibration relation, voltage markers, regional concentrations, regional volumes, and comparison inventory values [17]. The calculations are limited to those listed quantities, and the present contribution is the region-resolved voltage-window mass accounting developed from them.

Table 1. Quantitative measured inputs used for electrolyte-resolved voltage-gated inventory reconstruction.

Category	Value used in the reconstruction
Cathode formulation	$LiMn_2O_4$:PVdF:acetylene carbon black = 85:9:6 by mass
Cathode preparation	Slurry coated on aluminium foil; nominal active-material layer thickness of 75 µm; total electrode thickness of 59 µm
Carbonate liquid electrolyte	1 M $LiPF_6$ in EC:DMC, 1:1 by volume
Carbonate gel electrolyte	1 M $LiPF_6$ EC:DMC with PVdF-HFP polymer
Cyanoester electrolyte	1 M LiTFSI in methyl-3-cyanopropanoate (MCP)
Electrochemical protocol	Galvanostatic charging and discharging at ±25 µA
MRI conditions	^{1}H MRI at 9.4 T; two-dimensional spin-echo imaging
Calibration standards	$MnCl_2$ solutions at 0, 24, and 48 µmol L^{-1}
Calibration relation	$I = 3.6 \times 10^6 C_{Mn} + 53.547$, with C_{Mn} in mol L^{-1}
Voltage markers	Detectable intensity rise near 4.1 V; sharper release above approximately 4.7 V in carbonate electrolyte
Maximum mapped concentration	Approximately 36 µmol L^{-1} Mn^{2+} in the gel-electrolyte map
Regional concentrations	Cathode side: 28.6 µmol L^{-1}; middle: 22.1 µmol L^{-1}; anode side: 6.26 µmol L^{-1}
Regional volumes	Cathode side: 2.94×10^{-5} L; middle: 2.94×10^{-5} L; anode side: 13.5×10^{-5} L
Regional inventories	8.42×10^{-10}, 6.51×10^{-10}, and 8.45×10^{-10} mol in the cathode, middle, and anode-side regions
Total MRI-derived inventory	2.34×10^{-9} mol after one mapped cycle
ICP-AES comparison value	20.6×10^{-9} mol after three cycles

Table 1 establishes the experimental basis for the analysis. The entries span electrode composition, electrolyte chemistry, cell operation, imaging calibration, and regional concentration data. This broad set of inputs is necessary because manganese dissolution cannot be interpreted accurately from a single measurement category. The same concentration value can have different significance depending on its voltage origin and regional volume, while the same voltage response can have different consequences depending on whether released manganese remains near the cathode or migrates toward the negative electrode.

The table also defines the boundary of the present calculation. The reconstruction is deliberately tied to the listed cell conditions, voltage markers, calibrated concentration relation, and regional volumes. This prevents the analysis from becoming a general narrative about manganese dissolution and keeps the paper focused on its own research question: whether the measured MRI and electrochemical quantities can be assembled into a voltage-gated, region-resolved molar inventory.

The visual concentration standards used to define the MRI contrast scale are shown in Figure 1. The progressive change in vial appearance from 0 to 48 µmol L^{-1} demonstrates the concentration range over which dissolved Mn^{2+} produces a measurable imaging response. Figure 2 then connects this visual series to the linear calibration relation used in Eq. (1); together, the two figures justify treating the MRI intensity field as a quantitative concentration map rather than a qualitative contrast image.

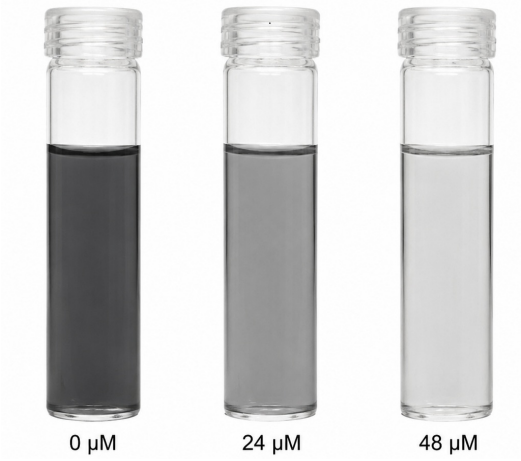

Figure 1. Visual Mn^{2+} calibration standards used to establish the micromolar concentration range for MRI interpretation. The 0, 24, and 48 µmol L^{-1} standards provide the reference contrast needed to relate proton MRI intensity to dissolved manganese content.

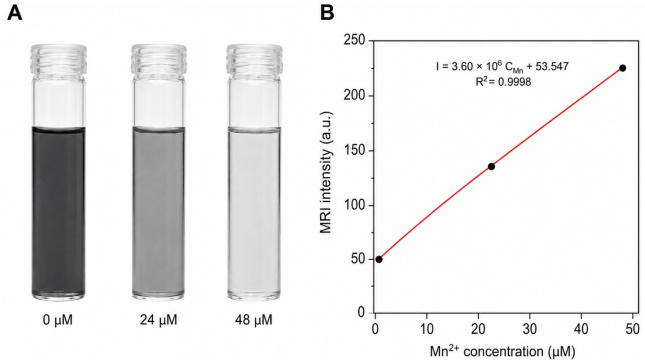

Figure 2. Calibration basis for converting MRI response into dissolved Mn^{2+} concentration. Panel A shows the standard solutions, while panel B gives the linear intensity–concentration relation used to calculate concentration fields from image intensity. The high linearity of the response supports quantitative interpretation within the measured micromolar range.

Figures 1 and 2 also define the reliability boundary of the subsequent analysis. The standards show that the mapped cell concentrations are evaluated inside the same micromolar interval used to create the calibration line. This matters because the derived inventory values in later sections depend directly on the validity of this signal-to-concentration conversion.

2.2 Conversion of MRI intensity to dissolved-manganese concentration

The first analytical step converts proton MRI intensity into dissolved Mn^{2+} concentration according to

$$C_{\mathrm{Mn}}(\mathbf{r}, t) = \frac{I(\mathbf{r}, t) - I_0}{S}, \tag{1}$$

where $I(\mathbf{r}, t)$ is the local image intensity, $I_0 = 53.547$ is the intercept, and $S = 3.6 \times 10^6$ is the calibration slope in intensity units per mol L^{-1}.

Eq. (1) is the chemical bridge between imaging and inventory analysis. It treats the MRI map as a quantitative concentration field rather than as a qualitative brightness pattern. The intercept represents the background electrolyte contribution under the calibration conditions, while the slope expresses the sensitivity of image intensity to micromolar Mn^{2+}. Because the standards extend to 48 µmol L^{-1}, the concentration values observed in the mapped cell lie within the same micromolar regime used for calibration.

The concentration range shown in Figures 1 and 2 is therefore matched to the reconstructed cell values. This alignment is important because it avoids extrapolating far outside the standard series and keeps the inventory calculation anchored to the measured MRI response.

2.3 Voltage-window assignment

The cell response is divided into four voltage domains:

$$\Omega(V) = \begin{cases} \Omega_{\mathrm{pre}}, & V < 4.1\,\mathrm{V}, \\ \Omega_{\mathrm{on}}, & 4.1\,\mathrm{V} \le V < 4.7\,\mathrm{V}, \\ \Omega_{\mathrm{acc}}, & V \ge 4.7\,\mathrm{V}, \\ \Omega_{\mathrm{dis}}, & \text{discharge branch.} \end{cases} \tag{2}$$

Eq. (2) introduces voltage as a gating variable. Ω_{pre} represents the region in which measurable manganese release is weak or absent. Ω_{on} captures the first detectable rise in MRI intensity and is interpreted as the onset of dissolution. Ω_{acc} represents the high-voltage region where the release rate increases more sharply. Ω_{dis} is separated because MRI intensity during discharge can reflect redistribution of already released Mn^{2+} as well as any continuing chemical reaction.

The same voltage-window logic is illustrated in Figure 3. The plotted concentration remains close to the lower micromolar regime below 4.1 V, increases through the intermediate charge region, and rises more rapidly once the cell enters the high-voltage domain at and above 4.7 V. This graphical separation provides the operating basis for assigning dissolution to onset and accelerated-release intervals.

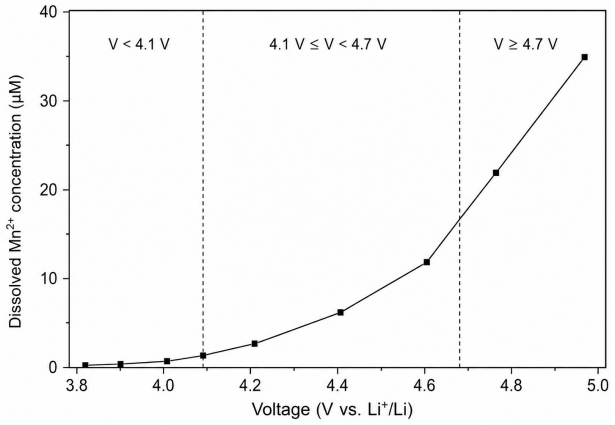

Figure 3. Voltage-gated interpretation of dissolved Mn^{2+} concentration. The low-voltage region below 4.1 V shows minimal release, the intermediate interval $4.1\,\mathrm{V} \le V < 4.7\,\mathrm{V}$ corresponds to measurable onset, and the region at $V \ge 4.7\,\mathrm{V}$ shows accelerated manganese dissolution.

Figure 3 converts the voltage profile into a materials interpretation. Below the onset gate, the cathode-electrolyte system remains below the imaging threshold for measurable release; between 4.1 V and 4.7 V, the first chemically meaningful dissolution signal appears; above 4.7 V, the response becomes steep enough to identify a separate high-voltage damage regime. This distinction is essential for answering the research question because it shows that the dissolution inventory is not uniformly accumulated over the whole charge step.

2.4 Regional inventory calculation

For a segmented electrolyte region k, the molar amount of dissolved manganese is calculated from

$$n_k = C_k\, V_k, \tag{3}$$

where C_k is the region-averaged concentration and V_k is the corresponding electrolyte volume. The total mapped inventory is

$$n_{\mathrm{map}} = \sum_{k=1}^{N} n_k. \tag{4}$$

Eqs. (3) and (4) define the core mass-accounting operation. They show why concentration and inventory must be distinguished. A small region with high concentration may contain the same number of moles as a larger region with lower concentration. This distinction is particularly important for interpreting transition-metal migration toward the negative electrode, where concentration may be diluted but molar exposure can still be meaningful.

2.5 Inventory descriptors

To compare regional distribution and transport, four descriptors are defined:

$$\Phi_k = \frac{n_k}{n_{\mathrm{map}}}, \tag{5}$$

$$P_{\mathrm{a/c}} = \frac{n_{\mathrm{anode}}}{n_{\mathrm{cathode}}}, \tag{6}$$

$$G_{\mathrm{c/a}} = \frac{C_{\mathrm{cathode}} - C_{\mathrm{anode}}}{C_{\mathrm{cathode}}}, \tag{7}$$

$$\chi_{\mathrm{ICP}} = \frac{n_{\mathrm{map}}}{n_{\mathrm{ICP}}}. \tag{8}$$

Φ_k gives the fraction of the mapped inventory located in region k. $P_{\mathrm{a/c}}$ compares the anode-side inventory with the cathode-side inventory and therefore measures the extent of molar propagation through the cell. $G_{\mathrm{c/a}}$ describes the remaining concentration gradient between release origin and anode-side volume. χ_{ICP} compares the one-cycle MRI-derived mapped inventory with the three-cycle ICP-AES inventory. These descriptors retain the raw concentration map while expressing it as degradation-relevant quantities for electrolyte screening and electrode-interface exposure. They also prevent a common misreading of imaging data: the brightest region is not automatically the region carrying the largest molar burden. A region with lower concentration can still contain a comparable number of moles when the sampled volume is larger, and this is precisely the condition encountered near the anode side of the mapped gel electrolyte.

3 Mechanistic Rationale

Manganese dissolution from $LiMn_2O_4$ is commonly associated with acid-assisted chemical attack and redox disproportionation. A simplified acid-assisted route may be written as

$$Li_{1-x}Mn_2O_4 + HF \longrightarrow \lambda\text{-}MnO_2 + LiF + Mn^{2+}_{\mathrm{solv}} + H_2O, \tag{9}$$

where the delithiated spinel surface reacts with acidic electrolyte species and produces solvated manganese.

Eq. (9) explains the vulnerability of $LiPF_6$-carbonate electrolytes. Even small amounts of water can contribute to salt decomposition and HF formation, and the high-voltage cathode surface is chemically more susceptible during delithiation. In the voltage-gated interpretation, the beginning of the intensity rise near 4.1 V corresponds to the point at which the electrochemical state of the cathode and the electrolyte environment become sufficiently reactive to produce detectable Mn^{2+}.

A complementary route is disproportionation of surface manganese:

$$2\,Mn^{3+}_{\mathrm{surface}} \longrightarrow Mn^{4+}_{\mathrm{surface}} + Mn^{2+}_{\mathrm{solv}}. \tag{10}$$

Eq. (10) connects lattice redox chemistry to soluble manganese generation. When the surface contains unstable Mn^{3+} sites, disproportionation can produce soluble Mn^{2+} even without complete structural collapse. The accelerated intensity increase above approximately 4.7 V is therefore interpreted as a regime in which high-voltage surface stress, electrolyte oxidation, and local manganese redox instability combine to increase the release flux.

Electrolyte chemistry controls both pathways. Carbonate–$LiPF_6$ environments can promote acidity and oxidative decomposition, whereas cyanoester–LiTFSI systems can reduce corrosive attack and modify the high-voltage interfacial environment. Gel electrolytes do not necessarily eliminate chemical release, but they reduce convective redistribution and therefore make spatial concentration fields easier to convert into regional inventories. The present method uses these differences not as qualitative labels but as measurable dissolution phenotypes.

The electrolyte contrast underlying this interpretation is shown in Figure 4. The carbonate liquid electrolyte gives the highest concentration response at elevated voltage, the carbonate gel electrolyte follows a similar but lower trajectory, and the cyanoester–LiTFSI MCP electrolyte maintains only a very small concentration increase. This comparison demonstrates that electrolyte formulation changes the release pathway itself, not only the final amount recovered after cycling.

Figure 4 provides the mechanistic bridge between electrolyte chemistry and voltage-window response. The carbonate liquid curve is consistent with a chemically permissive environment for manganese release, the gel carbonate curve preserves the release signature while limiting transport complexity, and the MCP–LiTFSI curve shows that the charge-window signal can be suppressed rather than merely redistributed. The figure is therefore used in the Results and Discussion as evidence of distinct dissolution phenotypes, not as a simple ranking of final concentrations.

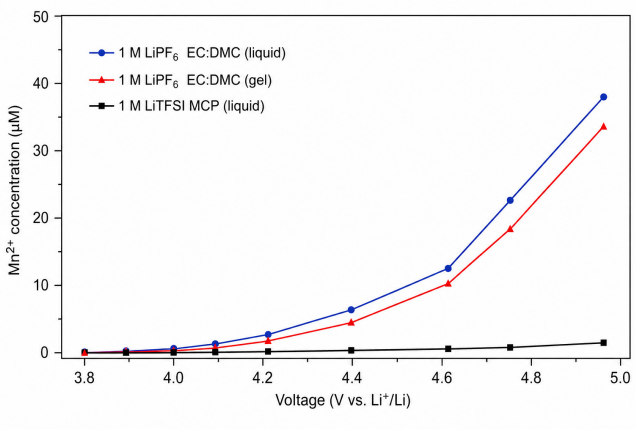

Figure 4. Electrolyte-dependent Mn^{2+} concentration response as a function of voltage. The 1 M $LiPF_6$ EC:DMC liquid electrolyte produces the strongest high-voltage manganese release, the corresponding gel electrolyte partially suppresses the concentration rise, and the 1 M LiTFSI MCP electrolyte strongly limits dissolved manganese over the same voltage range.

4 Results

4.1 Calibration response and MRI-based concentration conversion

The calibration relation in Table 1 transforms the proton MRI signal into a micromolar Mn^{2+} concentration scale. The inclusion of 0, 24, and 48 µmol L^{-1} standards is important because the mapped concentrations in the cell remain within a range where a linear conversion can be applied. In this sense, MRI does not only display the presence of dissolved manganese; it provides a spatially resolved analytical measurement that can be coupled to mass balance.

As shown in Figure 2, the calibration response is nearly linear across the standards. This supports the direct conversion of proton MRI intensity into Mn^{2+} concentration for the subsequent voltage-gated and region-resolved inventory calculations. The figure also gives practical meaning to the calibration equation: an increase in image intensity is not interpreted as brightness alone, but as a chemically scaled change in dissolved manganese concentration.

The calibrated concentration scale permits direct comparison between local MRI intensity, regional electrolyte volume, and independent chemical measurements. After calibration, a concentration maximum of about 36 µmol L^{-1} in the gel-electrolyte map can be compared with regional averages, electrolyte volume, and independent ICP-AES measurements. This conversion is the foundation for the inventory reconstruction presented below.

4.2 Voltage-gated manganese release during charge and discharge

The carbonate–$LiPF_6$ cell exhibits an observable increase in MRI intensity beginning near 4.1 V. This voltage is interpreted as the dissolution-onset gate because it marks the transition from a low-release region to a condition in which soluble Mn^{2+} becomes detectable. The onset is not treated as a single instantaneous event. Rather, it indicates that the delithiated cathode surface, the electrolyte salt environment, and the emerging acidic or oxidative species have reached a combination that permits measurable manganese release.

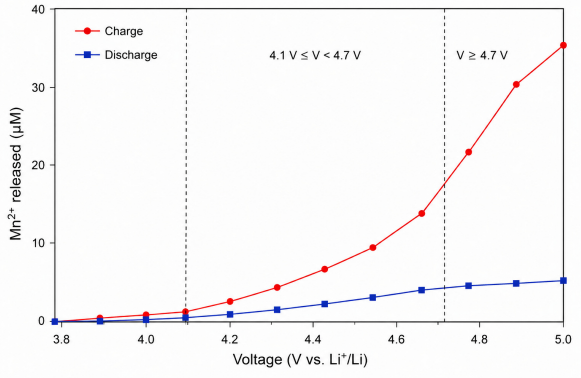

Figure 5. Charge–discharge separation of the Mn^{2+} response. The charge curve shows strong voltage-driven release, particularly near and above the high-voltage gate, whereas the discharge curve remains comparatively low, indicating that post-charge transport and retention should be distinguished from fresh high-voltage dissolution.

Above approximately 4.7 V, the intensity increase becomes stronger. This high-voltage interval is assigned to the accelerated-release gate. Figure 5 shows that the charge branch rises sharply through the onset and accelerated regions, whereas the discharge branch remains much lower and changes more gradually. This behaviour indicates that the dominant generation of dissolved Mn^{2+} is associated with charging at high voltage, while the discharge signal mainly reflects retention and redistribution of manganese already present in the electrolyte.

The discharge branch also carries transport evidence because intensity changes do not simply disappear when charging stops. Dissolved Mn^{2+} can remain in the electrolyte and continue to redistribute under concentration gradients, density differences, magnetic-field-related convection, or local interfacial interactions. Therefore, discharge images are interpreted as transport-retention evidence rather than as a clean measure of newly generated manganese.

4.3 Regional inventory reconstruction in the gel electrolyte

The gel-electrolyte configuration provides the clearest basis for regional inventory analysis because polymer-mediated immobilization reduces bulk convective mixing. The mapped gel-electrolyte maximum of approximately 36 µmol L^{-1} shows that manganese release remains chemically significant even when macroscopic redistribution is reduced. Regional averages and volumes were then used to calculate molar inventories.

Figure 6 shows the spatial segmentation used for this calculation. The cathode-side, middle, and anode-side reservoirs are assigned separate concentrations and volumes, allowing local concentration gradients to be converted into molar amounts.

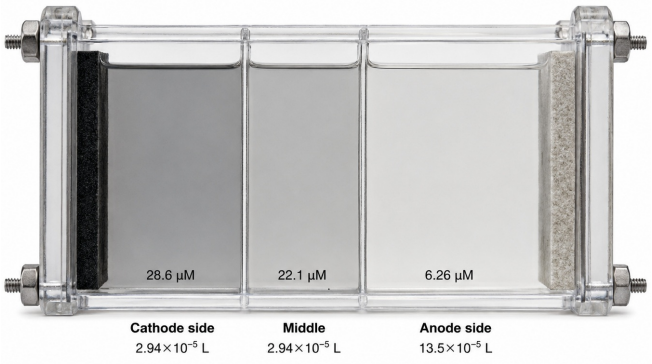

Figure 6. Region-resolved MRI inventory map for the gel-electrolyte cell. The cathode side, middle section, and anode side are treated as separate electrolyte reservoirs with measured Mn^{2+} concentrations and assigned volumes, enabling conversion from concentration to molar inventory.

Table 2. Regional concentration, volume, inventory, and distribution descriptors obtained by electrolyte-resolved voltage-gated inventory reconstruction.

Region or descriptor	Concentration µM	Volume L	Inventory mol	Inventory fraction Φ_k
Cathode-proximal region	28.6	2.94×10^{-5}	8.42×10^{-10}	0.360
Middle region	22.1	2.94×10^{-5}	6.51×10^{-10}	0.278
Anode-proximal region	6.26	13.5×10^{-5}	8.45×10^{-10}	0.361
Total mapped inventory	–	1.938×10^{-4}	2.34×10^{-9}	1.000
Equivalent mapped mean concentration	12.1	–	–	–
Anode/cathode propagation coefficient, $P_{a/c}$	–	–	1.00	–
Cathode/anode concentration contrast, $G_{c/a}$	–	–	0.781	–
MRI/ICP inventory comparison, χ_{ICP}	–	–	0.114	–

Table 2 shows that the cathode-proximal region has the highest local concentration, which is expected because manganese release originates at the cathode. The middle region has a lower but still substantial concentration, indicating that dissolved manganese moves beyond the immediate cathode vicinity during the mapped cycle. The anode-proximal concentration is much lower, but its larger sampled volume causes the anode-side inventory to become nearly equal to the cathode-side inventory.

The same result is visualized in Figure 7. The upper panel emphasizes the concentration gradient from the cathode-proximal region to the anode-proximal region, while the lower panel shows that the inventory fractions of the cathode-side and anode-side reservoirs are nearly identical.

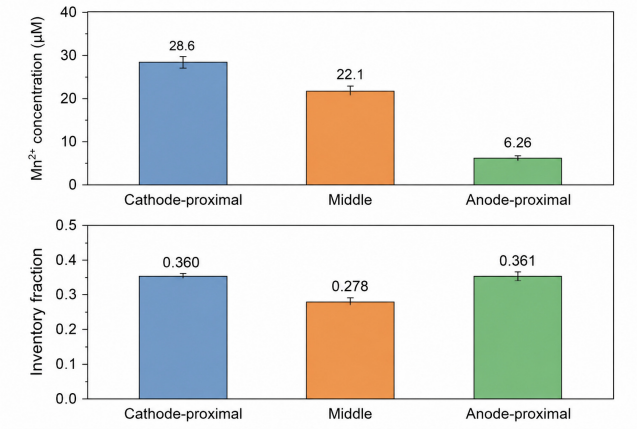

Figure 7. Regional Mn^{2+} concentration and inventory fraction in the segmented gel electrolyte. The cathode-proximal region has the highest concentration, but the anode-proximal region contains a comparable inventory fraction because of its larger sampled volume.

The one-cycle MRI-derived inventory is 2.34×10^{-9} mol, whereas the three-cycle ICP-AES comparison value is 20.6×10^{-9} mol. The resulting ratio is $\chi_{ICP} = 0.114$. Figure 8 summarizes this comparison between spatially resolved first-cycle mapping and bulk multi-cycle chemical recovery.

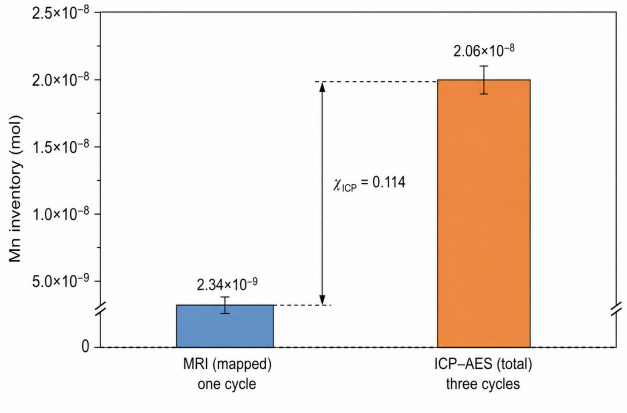

Figure 8. Comparison of mapped MRI-derived manganese inventory with the ICP-AES total inventory. MRI gives a spatially resolved first-cycle inventory of 2.34×10^{-9} mol, whereas ICP-AES gives a larger three-cycle total of 2.06×10^{-8} mol. The comparison coefficient $\chi_{ICP} = 0.114$ indicates the scale relation between the two analytical domains.

4.4 Electrolyte-dependent dissolution phenotype

The carbonate liquid electrolyte, carbonate gel electrolyte, and cyanoester electrolyte display distinct manganese-release behaviours. Figure 4 shows these differences directly as voltage-dependent concentration trajectories, while their materials interpretation is summarized in Table 3.

Table 3. Electrolyte-dependent manganese-dissolution phenotypes interpreted by the inventory-reconstruction method.

Electrolyte condition	Observed response	Materials interpretation
1 M $LiPF_6$ EC:DMC liquid	Charge-window intensity rises and signal redistributes during discharge	Manganese release is detectable, but liquid-phase motion complicates strict regional inventory assignment
1 M $LiPF_6$ EC:DMC gel	Maximum mapped concentration near 36 μmol L^{-1}; regional inventories can be calculated	Gel immobilization limits convective spreading and enables quantitative spatial manganese accounting
1 M LiTFSI MCP	Charge-window intensity increase is strongly suppressed, with only slight discharge-branch change	Cyanoester–LiTFSI chemistry suppresses voltage-triggered manganese release and reduces the corrosive dissolution phenotype

Table 3 demonstrates that electrolyte formulation affects more than the final amount of manganese detected after

cycling. In the liquid carbonate electrolyte, release is visible but spatial quantification is more difficult because dissolved species can redistribute strongly. In the gel carbonate electrolyte, manganese release remains visible, but the suppressed convective component allows the dissolved inventory to be partitioned region by region. In the cyanoester–LiTFSI electrolyte, the charge-window response is strongly attenuated, indicating that the electrolyte prevents or delays the chemical conditions that generate detectable Mn^{2+} during charging.

5 Discussion

5.1 Quantitative interpretation of calibrated MRI

This calibrated interpretation adds to the connection between Table 1 and the figures. The former gives the mathematical relation, while Figures 1 and 2 demonstrate the reasoning behind the relation's applicability in micromolar concentrations. In this way, the reader is taken through the process from the concentration of Mn^{2+} in solution to its intensity representation in an image and finally to its inventory calculation, without having to encounter the leap from one to another in the form of just equations.

Calibration is especially important when comparing qualitative with quantitative MRI interpretations. A bright spot in the MRI image implies more Mn^{2+} dissolution, which causes greater modification of the relaxation processes in the field of view, but it does not tell whether the difference is chemically significant or minor. Once calibration is applied, the image becomes a concentration map from which the manganese inventory can be recovered rather than just a description of intensity contrast.

5.2 MRI voltage gating of manganese dissolution

The separation of voltage ranges in Figures 3, and 5 shows clearly why it is necessary. The high voltage contributes significantly more to manganese loss during cycling than the average value over the entire charging profile might imply. By distinguishing the voltage regions, it becomes clear that manganese is released not during the entire charging phase but rather during the higher voltage windows that lead to increased instability at surfaces and in the electrolyte.

This distinction is confirmed by Figure 5, since the response of the discharge branch is not equivalent to that of the charge branch. Instead, the much lower but nonzero discharge signal is consistent with transported manganese. In this sense, the charge-discharge comparison confirms the voltage-based analysis of the research question, demonstrating that the majority of manganese loss occurs during high-voltage charging and that discharge is only responsible for carrying pre-existing manganese.

This is crucial for interpreting discharge-branch MRI signals as evidence of manganese transport and accumulation rather than of manganese dissolution and release. Charge signals are therefore used to identify voltage windows that contribute to manganese loss and to distinguish between release and redistribution processes. This separation is important in developing proper mitigation strategies.

5.3 Meaning of the regional inventory reconstruction

The near-equal inventory fractions for the cathode- and anode-side reservoirs indicate why it is important to go beyond concentration maps. Specifically, the cathode-side inventory fraction is 0.360, while the anode-side inventory fraction is 0.361, and these are not just two identical concentration values. The concentration contrast $G_{c/a} = 0.781$ confirms that there is still a steep gradient in the field of view from cathode to anode, so molar exposure and concentration exposure are distinct quantities.

In terms of long-term degradation and cell design, the anode-side manganese inventory plays a vital role, since transition-metal-containing species can reach the negative electrode and influence interphase reactions, despite a relatively low local concentration. In addition to providing the concentration gradient, the regional descriptors listed in Table 2 show why anode-side measurement is not just a secondary observation. On the one hand, $G_{c/a} = 0.781$ means that release originates from the cathode side. On the other hand, $P_{a/c} = 1.00$ shows that both regions contain roughly equal molar exposures. This is a key inventory result of the paper because source identification and molar exposure evaluation require different quantities.

Finally, no direct conflict exists between the results of MRI and ICP-AES measurements, although it may seem so at first. In fact, the comparison highlights an important point about their complementary nature. While MRI yields a concentration map of an initial charge cycle, ICP-AES samples multiple cycles of manganese dissolution. The comparison is nevertheless valuable because it demonstrates that the MRI-inferred manganese value is within an appropriate order of magnitude and can be spatially localized better than bulk ICP-AES.

5.4 Suppression of high-voltage manganese release by electrolyte chemistry

The near-flat MCP response in Figure 4 is especially significant in this context. Indeed, it indicates that electrolyte chemistry can modify the manganese dissolution phenotype such that manganese release occurs no longer due to voltage gates but to a more robust high-voltage resistance. In other words, the MCP–LiTFSI electrolyte not only changes the pattern of concentration distribution but reduces manganese release, which requires a different treatment of electrolytes in materials design.

More specifically, the cyanoester-based electrolyte should be viewed as representing an alternative design philosophy relative to the gel-based electrolyte. Indeed, unlike the latter, cyanoester-based electrolyte does not simply immobilize manganese; it shifts the voltage gating of manganese release to the region of very high voltages where release hardly occurs anyway. In this respect, Table 3 provides the following rule for electrolyte design: electrolytes with carbonate system require controlling acid-assisted release and high-voltage release; gel electrolytes help manage the regional transport of manganese and increase spatial interpretability; and MCP–LiTFSI electrolytes are useful if they suppress release in the voltage gates.

5.5 Consequences of manganese dissolution and materials-design implications

The reconstructed inventory provides a mechanistic explanation of why manganese dissolution can be problematic beyond the loss of cathode-active material. Indeed, the concentration contrast $G_{c/a} = 0.781$ confirms that manganese release starts near the cathode. However, the anode-side molar exposure is comparable, which implies that the negative electrode is exposed to transition metals. This conclusion has important consequences for long-term cell performance since subsequent cycles of manganese dissolution can lead to deposition and participation in interphase reactions.

From a materials-design perspective, the inventory-based analysis suggests that it would be worth modifying the charging protocol because of the voltage dependence of manganese release. In particular, Figure 5 shows that the strongest release signal corresponds to voltage values above 4.7 V, which means that keeping out of this high-voltage range could reduce manganese release. Similarly, an electrolyte containing an additional additive should be assessed based not just on final concentration reduction but also on voltage gating of manganese dissolution. Specifically, it should prevent manganese release during the onset (G region) or acceleration (H region) voltage gates.

These observations imply that capacity retention tests should be complemented by diagnostic tools that specify which voltage range and region are responsible for manganese dissolution. In other words, while a cathode coating with reduced manganese release at high voltage, an electrolyte with delayed voltage gate, and a gel matrix preventing diffusion will all result in similar overall concentration values, these options have very different risk profiles in terms of materials design. The inventory method distinguishes these cases by reporting voltage gating, concentration gradients, and molar exposures simultaneously.

As an added benefit, the inventory method can help in identifying materials-design criteria related to high-voltage manganese release. In particular, it can be used to assess effectiveness of various cathode coatings, electrolyte salts, solvents, separators, and gel/polymer electrolytes. All of these materials should be tested based not just on capacity retention but also on molar exposure and voltage gating.

5.6 Strengths and weaknesses of the method, and future research directions

The principal strength of the inventory method is its ability to combine concentration maps with voltage information. Moreover, it can additionally provide spatial location data to supplement bulk chemical measurements. Together, these four pieces of information answer the most complete degradation question by identifying the cathode origin, voltage gating, high molar inventory at the anode, and distinct electrolyte chemistries that can release, immobilize, or suppress manganese dissolution.

A major weakness is that the inventory reconstruction depends on the concentration relation, segmentation, and volumes of segmented regions. More generally, this method relies on the assumption that the relation applies under electrolyte-specific conditions. Since MRI and ICP-AES test different cell cycles, their inventories cannot be compared directly, and the values should be treated as complementary. Another weakness is that inventory reconstruction is performed based on the published data, so a more detailed analysis would involve voltage-gating experiments followed by image acquisition and chemical measurement at each hold.

For example, the following quantity can be introduced to capture the voltage-dependent dynamics:

$$R_j = \frac{n_{\mathrm{map}}(t_{j+1}) - n_{\mathrm{map}}(t_j)}{t_{j+1} - t_j}, \tag{11}$$

where R_j is the inventory growth rate in the jth voltage window.

This would turn the inventory reconstruction tool into a kinetics study that identifies dominant voltage windows with high R_j values, which correspond to high-voltage manganese release. At the same time, small values of R_j in a protected

electrolyte would show successful manganese retention. These observations can be used to compare various cathode coatings, electrolyte salts, solvent families, and polymer matrices.

6 Conclusion

This paper asked whether manganese dissolution from spinel $LiMn_2O_4$ can be reconstructed as a voltage-gated and region-resolved inventory process rather than as a single bulk concentration or qualitative MRI contrast change. The answer is yes. The calibrated MRI response, voltage-window assignment, and regional inventory calculation show that dissolution begins as a detectable process near 4.1 V, intensifies above approximately 4.7 V, and produces a spatial distribution whose degradation significance cannot be understood from concentration alone.

The methodological finding is that proton MRI can be converted into a quantitative degradation map when the signal is calibrated against known Mn^{2+} standards. Eq. (1) supplies the concentration field, Eq. (2) assigns that field to electrochemical voltage domains, and Eqs. (3) and (4) convert regional concentrations into molar inventories. The descriptor set in Eqs. (5)–(8) then translates the map into distribution, propagation, concentration contrast, and comparison quantities. Thus, the paper's contribution is not simply the recognition that manganese dissolves; it is the reconstruction of when, where, and how much manganese is present during the mapped process.

The main quantitative result is that the gel-electrolyte map reaches a maximum concentration of approximately $36\,\mu mol\,L^{-1}$ and gives a first-cycle mapped inventory of 2.34×10^{-9} mol. The cathode-side, middle, and anode-side inventories are 8.42×10^{-10}, 6.51×10^{-10}, and 8.45×10^{-10} mol, respectively. The cathode side has the highest concentration, confirming the positive electrode as the dissolution origin, but the anode-side sampled region contains essentially the same molar inventory because its volume is larger. This resolves the paper's central spatial question: anode-side risk cannot be dismissed by observing a lower local concentration, because molar exposure depends on both concentration and volume.

The voltage-domain result is equally important. Figures 3 and 5 show that the dominant generation of soluble Mn^{2+} occurs during charge and is concentrated in the onset and accelerated high-voltage windows. The discharge response is lower and is better interpreted as persistence and redistribution of dissolved manganese than as a comparable fresh-release process. This conclusion gives a practical operating implication: limiting residence in the high-voltage accelerated-release domain should reduce manganese dissolution, while diagnostic evaluation of cathode or electrolyte modifications should report the voltage interval in which protection occurs.

The electrolyte result answers the materials-design part of the research question. Carbonate–$LiPF_6$ promotes a clear voltage-window release phenotype, the carbonate gel retains measurable release while improving regional interpretability, and MCP–LiTFSI strongly suppresses the charge-window intensity rise. The protective behaviour of MCP–LiTFSI is therefore interpreted as chemical suppression of the release pathway rather than simple dilution or delayed transport. For electrolyte development, successful formulations should be judged by their ability to suppress the onset gate and the accelerated high-voltage gate, not only by lowering the final dissolved-manganese concentration after cycling.

Overall, the interpretation links cathode redox instability, salt and solvent chemistry, magnetic-resonance calibration, and regional mass accounting into a single degradation diagnosis. The approach can be applied to voltage-hold imaging, repeated-cycle mapping, cathode coatings, alternative salts, modified separators, and gel or polymer electrolytes. Its broader value is that it converts spatial imaging into a materials-engineering decision tool: the safest electrolyte or electrode design is the one that minimizes voltage-triggered release, limits migration toward the negative electrode, and lowers the molar inventory available to damage cell interfaces.

Data Availability

All numerical values used in the analysis are given in the tables and equations of this manuscript. The reconstruction can be reproduced from the calibration relation, voltage markers, region concentrations, region volumes, and inventory values listed in Table 1.

Conflict of Interest

The authors declare no conflict of interest.

References

[1] Y. Gao and J. R. Dahn, "Correlation between the growth of the 3.3 V discharge plateau and capacity fading in $Li_{1+x}Mn_{2-x}O_4$ materials," *Solid State Ionics*, vol. 84, pp. 33–40, 1996.

[2] S. J. Wen, T. J. Richardson, L. Ma, K. A. Striebel, P. N. Ross, and E. J. Cairns, "FTIR spectroscopy of metal oxide

insertion electrodes: a new diagnostic tool for analysis of capacity fading in secondary Li/$LiMn_2O_4$ cells," *Journal of The Electrochemical Society*, vol. 143, pp. L143–L146, 1996.

[3] D. H. Jang and S. M. Oh, "Electrolyte effects on spinel dissolution and cathodic capacity losses in 4 V Li/$Li_xMn_2O_4$ rechargeable cells," *Journal of The Electrochemical Society*, vol. 144, pp. 3342–3348, 1997.

[4] D. H. Jang, Y. J. Shin, and S. M. Oh, "Dissolution of spinel oxides and capacity losses in 4 V Li/$Li_xMn_2O_4$ cells," *Journal of The Electrochemical Society*, vol. 143, pp. 2204–2211, 1996.

[5] L. F. Wang, C.-C. Ou, K. A. Striebel, and J. S. Chen, "Study of Mn dissolution from $LiMn_2O_4$ spinel electrodes using rotating ring-disk collection experiments," *Journal of The Electrochemical Society*, vol. 150, pp. A905–A911, 2003.

[6] Y. Terada, Y. Nishiwaki, I. Nakai, and F. Nishikawa, "Study of Mn dissolution from $LiMn_2O_4$ spinel electrodes using in situ total reflection X-ray fluorescence analysis and fluorescence XAFS technique," *Journal of Power Sources*, vol. 97–98, pp. 420–422, 2001.

[7] K. Leung, "First-principles modeling of the initial stages of organic solvent decomposition on $Li_xMn_2O_4$(100) surfaces," *Journal of Physical Chemistry C*, vol. 116, pp. 9852–9861, 2012.

[8] R. Benedek, "Role of disproportionation in the dissolution of Mn from lithium manganate spinel," *Journal of Physical Chemistry C*, vol. 121, pp. 22049–22053, 2017.

[9] S. Chandrashekar, N. M. Trease, H. J. Chang, L.-S. Du, C. P. Grey, and A. Jerschow, "^{7}Li MRI of Li batteries reveals location of microstructural lithium," *Nature Materials*, vol. 11, pp. 311–315, 2012.

[10] M. Klett, M. Giesecke, A. Nyman, F. Hallberg, R. W. Lindstrom, G. Lindbergh, and I. Furo, "Quantifying mass transport during polarization in a Li ion battery electrolyte by in situ ^{7}Li NMR imaging," *Journal of the American Chemical Society*, vol. 134, pp. 14654–14657, 2012.

[11] M. M. Britton, P. M. Bayley, P. C. Howlett, A. J. Davenport, and M. Forsyth, "In situ, real-time visualization of electrochemistry using magnetic resonance imaging," *Journal of Physical Chemistry Letters*, vol. 4, pp. 3019–3023, 2013.

[12] J. M. Bray, A. J. Davenport, K. S. Ryder, and M. M. Britton, "Quantitative, in situ visualization of metal-ion dissolution and transport using ^{1}H magnetic resonance imaging," *Angewandte Chemie International Edition*, vol. 55, pp. 9394–9397, 2016.

[13] J. P. Allen, C. A. O'Keefe, and C. P. Grey, "Quantifying dissolved transition metals in battery electrolyte solutions with NMR paramagnetic relaxation enhancement," *Journal of Physical Chemistry C*, vol. 127, pp. 9509–9521, 2023.

[14] S. Brox, M. Winter, T. Placke, and co-workers, "Alternative single-solvent electrolytes based on cyanoesters for safer lithium-ion batteries," *ChemSusChem*, vol. 9, pp. 1704–1711, 2016.

[15] S. Brox, M. Winter, T. Placke, and co-workers, "Innovative, non-corrosive LiTFSI cyanoester-based electrolyte for safer 4 V lithium-ion batteries," *ChemElectroChem*, vol. 4, pp. 304–309, 2017.

[16] K. Xu, "Electrolytes and interphases in Li-ion batteries and beyond," *Chemical Reviews*, vol. 114, pp. 11503–11618, 2014.

[17] N. Hellar, Y. Iwai, M. Ohzu, S. Brox, A. Dorai, R. Takekawa, N. Kuwata, J. Kawamura, and M. Winter, "Direct observation of Mn-ion dissolution from $LiMn_2O_4$ lithium battery cathode to electrolyte," *Communications Materials*, vol. 6, article 23, 2025.